INT. J. REMOTE SENSING, 1993, VOL. 14, NO. 2, 275-294

Radar imaging of thermal fronts

F. ASKARI, G. L. GEERNAEFT†, W. C. KELLER

Center for Advanced Space Sensing, U.S. Naval Research Laboratory, Washington, D.C. U.S.A.

and S. RAMAN

Department of Marine, Earth and Atmospheric Sciences, North Carolina State University, Raleigh, North Carolina, U.S.A.

(Received 22 July 1991; in final form 19 November 1991)

Abstract. The paper investigates the physics of radar backscatter across sea surface temperature fronts using a simple drag model followed by actual airborne radar observations. The model predicts large changes in radar cross section for low wind speed conditions. The X-band (9·43 GHz) Real Aperture Radar (RAR) observations in the vicinity of the sea surface temperature fronts show that radar cross-section variations are largely dependent on the local wind direction with respect to the front and the change in wind stress response at the front and feedbacks from the larger scale buoyancy driven circulation. Other radar imaging mechanisms are discussed.

1. Introduction

Ocean fronts are regions where dynamical, biological and chemical properties change abruptly, and exploring their nature and description is a key element in understanding acoustic propagation, exploiting fisheries potential, describing ocean heat transport, and study mesoscale ocean dynamics. Passive and active remote sensing techniques can be readily used to map the surface manifestation of ocean fronts by detecting changes in sea surface temperature, ocean colour and surface roughness. For active systems and in particular radar imagery, variations in image intensity or radar reflectivity correspond to variations in surface roughness.

Experiments using radar to extend our understanding of fronts and eddies have been conducted for nearly two decades. Weissman and Thompson (1977), Hayes (1981), Ross (1981), Lichy *et al.* (1981) discovered that the Gulf Stream front and warm core rings in general appear to have a brighter image tone or higher over all cross-section relative to the adjacent shelf or ambient waters. Fu and Holt (1983) identified a cold core eddy in the Grant Banks region from curvilinear streaks and mottled texture changes in Seasat-SAR image intensity. Similar patterns were observed by Cheney (1981) but with much weaker tonal signatures. During the Frontal Air Sea Interaction Experiment (FASINEX) conducted in February 1986, the first comprehensive set of measurements (by NRL and JPL investigators) were collected over Gulf Stream sea surface temperature (SST) fronts during a wide range of environmental conditions (Stage and Weller 1985, 1986). The general consensus from the above studies is that the changes in atmospheric stratification resulting from changes in sea surface temperature caused the change in the surface wind

†Now at Office of The Chief of Naval Research, Arlington, VA, U.S.A.

0143-1161/93 $10.00

stress; hence the change in surface roughness driven by the stress variability is one of the dominant ingredients in the imaging of mesoscale frontal boundaries.

Much of the radar related data complementing ocean observations has been a qualitative description of changes in SAR image intensity associated with mesoscale phenomena. In principal, the SAR imaging instrument is a sum of RAR and the phase history of the scattering element; where the RAR measures the amplitude of the Radar Cross Section (RCS)). Hence, absolute RCS measurements and quantitative information on the myriad of physical processes responsible for the step-change in cross-section significantly contributes to the understanding of SAR imaging of mesoscale ocean features. Since wind stress dominates the physical processes governing radar backscatter, one can presently provide coarse estimates of wind stress gradients over SST fronts using spatial images of radar returns. As we will see in §2, the theory supporting wind stress estimates requires spatial homogeneity and stationarity; regions which contain SST fronts unfortunately are often highly heterogeneous.

For this study, a nadir looking radiometer (PRT-5) is used in conjunction with an imaging radar to investigate the mapping of thermal ocean fronts. We will show that under some atmospheric stability conditions the absolute position of a thermal front as detected from an airborne radiometer (PRT-5) does not necessarily coincide with the position of a RCS or roughness front, and in fact one can lead or lag the other, in particular during low wind speeds. In §2 the theoretical framework for explaining the radar cross-section variations across thermal fronts is formulated. Section 3 covers two separate case studies of radar imaging of thermal fronts in the Gulf Stream region of the east coast of the U.S. In §4, a brief descriptive account of relevant boundary layer physics and discussion of results is given followed by conclusions in §5.

2. Theoretical background

The prevailing model which best describes radar ocean backscatter in the microwave region is composite surface theory based on Bragg resonant scattering, see e.g., Plant (1990). The theory can be applied to the ocean surface such that if one can model the energetics of Bragg resonant ocean surface waves, i.e., derived from the balance between wind stress, dissipation, and wave-current interactions, the radar backscatter can be simulated at any given point in space or time (see Plant 1986, Donelan and Pierson 1987). However, to tackle this problem practically in oceanic regions having SST fronts, the components to short wave energy balance must be parameterized in terms of easily measured atmospheric and oceanic information, e.g., local wind speed, atmospheric stability, currents, surface tension, water depth, and upwind fetch.

In the case of RAR cross-section, changes over SST fronts of small horizontal width (order of 1 km), the change in atmospheric stability is the primary bulk quantity undergoing an immediate response to the change in sea surface temperature. (Note that wind stress is not considered here to be a bulk quantity.) Combined with a nearly constant windspeed, this change in stability imparts a change in surface wind stress which, in turn induces a change in Bragg surface slope and energetics. It is this change in Bragg wave slope which, in most part, causes a change in radar cross-section. Traditionally, the normalized radar cross-section σ_0 has been related to wind velocity U, by a simple power law relation $\sigma_0 = AU^B$ where, A and B are empirical constants (see, Schroeder *et al.* 1982). Using measurements collected over

several years and from a variety of sites, Keller *et al.* (1989) suggested that the inclusion of atmospheric stability as an additional parameter in the scatterometer model function could produce better accuracies and more global applicability than the early model functions. Geernaert (1990 a) additionally suggested that replacing 'windspeed and stability' in the scatterometer model function with 'wind stress' would produce a more physically consistent model function where stability effects on radar cross-section disappear; using wind stress as the predicted parameter additionally satisfies the scientific requirement for more accurate oceanographic circulation model capabilities where wind stress and wind stress curl are two key parameters of interest. The results of Li *et al.* (1989) and Geernaert *et al.* (1988) have also suggested that the cross-section is fundamentally related to the local wind stress, and that the scatterometer model function relates to wind speed only through the latter's relationship with wind stress. The power law exponent which defines radar cross-section with wind stress generally depends on incidence angle, radar frequency, and polarization and is empirically written as:

$$\sigma_0(\mathrm{dB}) = A + 10B \log u^{2*} \tag{1}$$

where u^* is friction velocity. In the case of Ku-band, V-pol, at 45° incidence angle, $B = 0{\cdot}88$, and $A = -26{\cdot}7$, where units are in dB and m sec^{-1} (based on Keller *et al.* 1989).

In order to predict the behaviour of u^* using environmental variables, we must first examine the nature of the windspeed profile. For neutral stratifications, the wind profile varies logarithmically with height:

$$U(z) = \frac{u^*}{k}\left[ln\left(\frac{z}{z_0}\right)\right] \tag{2}$$

where U is the mean wind speed at height z, k is the von Karman constant ($=0{\cdot}4$), and z_0 is the roughness length.

To account for stability variations the profile is adjusted by a stability function β, such that (Geernaert 1990 b),

$$U(z) = \frac{u^*}{k}\left[ln\left(\frac{z}{z_0}\right) - \beta\right] \tag{3}$$

The function β is positive for stable flow, zero for neutral conditions, and negative for unstable stratifications.

Using (2) and (3), the change of wind stress over a sea surface temperature front can be estimated by assuming that atmsopheric mean quantities exhibit the same values on both sides of the front, and using the bulk aerodynamic relation (3), the stability adjustment is manifested in the drag coefficient, i.e.,

$$u^{2*} = C_D U^2 \tag{4}$$

where, the drag coefficient C_D, depends on the sampling height, z, atmospheric stratification, β, and the wave state influence on the roughness length, z_0, i.e.,

$$C_D = \left[\frac{0{\cdot}4}{ln\left(\frac{z}{z_0}\right) - \beta}\right]^2 \tag{5}$$

The quantity, β, can be approximated by using bulk information on surface layer windspeed and temperature, T, at 10 m height and surface temperature, T_s, (see Geernaert 1990a):

$$\beta = \frac{0{\cdot}14bf(T-T_s)}{U^2 C_D^{1{\cdot}5}} \tag{6}$$

where $bf = 0{\cdot}0067$, for $(T-T_s)<0$; and $bf = 0{\cdot}0040$, for $(T-T_s)>0$; these values are based on evaluations provided by Smith (1980) and Geernaert, (1990b). For simplicity, we will treat z_0 as a constant of 10^{-4} m, and the drag coefficient can to first order be determined iteratively, i.e.,

$$C_D = \left[\frac{0.4}{11{\cdot}55 - \frac{0{\cdot}14bf(T-T_s)}{U^2 C_D^{1{\cdot}5}}}\right]^2 \tag{7}$$

Combining (1), (4), (5) and (6), the change in cross-section across a SST front becomes:

$$\Delta\sigma_0 = B_d \log C_{D_d} - B_u \log C_{D_u} + [B_d - B_u] \log U^2 \tag{8}$$

where lower case subscripts 'd' and 'u' denote downwind and upwind of the SST front, respectively. For the simplified case of constant wind over a sharp SST front where the ambient windspeed remains steady and constant, with $B_d = B_u$, (8) reduces to:

$$\Delta\sigma_0 = B \log\left[\frac{C_{D_d}}{C_{D_u}}\right] \tag{9}$$

Equations (8) and (9) are based on the assumption that σ_0 can be adequately described by u^* and secondary effects such as viscosity are relatively unimportant.

Based on wave tank and field measurements (Keller and Plant 1988, Keller *et al.* 1989), parameterizing σ_0 on u^* works well over both homogeneous and inhomogeneous regions as long as u^* is greater than $0{\cdot}15\,\mathrm{m\,s^{-1}}$ (or neutral wind speed is above $4\,\mathrm{m\,s^{-1}}$) and the footprint is large enough that the wind field and surface interact as a stationary process. For u^* above $0{\cdot}15\,\mathrm{m\,sec^{-1}}$, B can be treated as a constant with magnitude near unity and similarly the cross-section follows a simple empirical dependence on u^*.

For values of u^* below $0{\cdot}15\,\mathrm{m\,sec^{-1}}$ (corresponding to neutral windspeeds below $4\,\mathrm{m\,sec^{-1}}$), theoretical predictions of the model function dependence on wind speed (Plant 1986; Donelon and Pierson 1987) suggest dramatic restrictions on the operational use of (1), (8), and or (9). Keller and Plant (1988) indicated that below $4\,\mathrm{m\,s^{-1}}$ the magnitude of B is inversely dependent on u^2 and that the presence of long waves acts to lower the value of B relative to the absence of long waves. For wind speeds below $2\,\mathrm{m\,s^{-1}}$ one could expect B to be at least an order of magnitude larger than for wind speeds above $4\,\mathrm{m\,s^{-1}}$. After re-examining the data reported by Keller and Plant (1988) applicable to the low wind regime of u^* less than $0{\cdot}15\,\mathrm{m\,sec^{-1}}$, we find that B follows an empirical form such that,

$$B = \left[\frac{0{\cdot}15}{u^*}\right]^2 ; \; u^* < 0{\cdot}15\,\mathrm{m\,s^{-1}} \tag{10}$$

Combining (10) with (1), an alternative form of (9) applicable to low winds is

$$\Delta\sigma_0 = \log\left[\frac{C_{D_d}B_d}{C_{D_u}B_u}\right] + [B_d - B_u]\log U^2;\ u^* < 0{\cdot}15\,\mathrm{m\,s^{-1}} \tag{11}$$

Note that since B depends on u^*, different values of B must be applied to the two sides of the SST front. Using (9) and (11), one can now estimate $\Delta\sigma_0$ given observed bulk wind speeds and air-sea temperature differences. For illustration, let wind blow from the colder surface side of a temperature front of $\Delta T = 6°C$. On the upwind side the atmospheric surface layer is stably stratified, while on the downwind side it is unstable. Letting the wind speed for these simulations be 2, 3, 4, and $5\,\mathrm{m\,s^{-1}}$, respectively, we calculate $\Delta\sigma_0$ to be 45, 3, 1, and 0·4 dB. While the magnitude of observed $\Delta\sigma_0$ should be large in the low wind regimes, great uncertainty in the predicted $\Delta\sigma_0$ should be kept in mind in most part since both (5) and (11) will exhibit an increasing influence of local scale circulations which will change the spatial pattern of winds near the sea surface temperature fronts. Local circulations are induced by pressure gradients set up over the SST front which result in wind fronts occurring at positions both upwind and downwind of the SST front. Therefore, for the low windspeed case, one should expect to find sharp gradients of cross-section associated with wind fronts and the low level circulation away from the SST front. We will elaborate on the role of such circulations in interpreting RAR images in §4.

3. Experiment

In April 1989, the Naval Research Laboratory performed two separate airborne surveys of SST fronts off the coast of Virginia and Maryland. In order to test the RAR's imaging response to the stability induced gradients of radar cross-section across SST fronts; both experiments were chosen to be in an oceanographic region where the surface temperature variability was significantly large. The first set of measurements were taken on 13 April in the Gulf Stream region at approximately 74° W and 37° N. The same area was revisited on 25 April and radar imagery were collected over what appeared to be a warm core ring structure.

3.1. *Environmental background*

Data from the Advanced Very High Resolution Radiometer (AVHRR) imagery from the NOAA-11 polar orbiting satellite with nominal 1·1 km resolution was obtained for the SST analysis during the 13 April and 25 flights. Due to the lack of ground truth during these experiments, namely open ocean wind stress measurements, whether maps from the National Meteorological Center (NMC) were used to estimate the wind speeds and directions.

3.1.1. *Case 1: 13 April 1989*

The survey area is shown on the AVHRR image (figure 1). The survey pattern was designed to cross the SST front on four separate occasions and at different look directions. The north edge of the Gulf Stream front is estimated to be located along the 74° 30′ latitude and zonally along the 37° latitude. Below the latitude 36° 15′ there is extensive cloud cover.

At 18.00 GMT on 13 April, geostrophic winds are from the north-northwest at $5\text{-}7\,\mathrm{m\,s^{-1}}$ due to a low pressure trough situated just to the east of the study area (figure 2). During the period 17.00 and 18.30 GMT, data recorded by the NRL P-3

inertial navigation system showed winds at 8·5 m s^{-1} from 340° at 1000 m flight altitude.

3.1.2. *Case 2: 25 April 1989*

Due to extensive cloud cover on 25 April, the satellite imagery on 24 April was used to show the survey area (figure 3). The imagery shows a warm core ring structure centred at 74° W and 37° N, with curvilinear temperature bands ranging from 13° to 18°C. The Gulf Steam front appears to the south and east of the area and was not included in the survey. The NRL P-3 flight plan was designed such that the warm core ring surface temperature front could be crossed nine times. Of the nine passes, four crossings show a temperature jump in excess of 6°C over a distance of approximately 3 km, while the remaining five frontal crossings exhibited weak linear temperature changes in the neighbourhood of 2°C.

The meteorological conditions during the flight survey on 25 April were dominated by a low pressure system centred on 65° W, 45° N. The low's 1012 mb isobar ran perpendicular to the New Jersey coast. A stationary front was situated off the Norfolk coast just to the south of the survey area (figure 4). The 18.00 GMT surface data shows a moderate (7·5 m s^{-1}) westerly wind from approximately 280° at 35·8° N, 71° W. For the same time period, a light southerly wind field (from 180) with a speed of a 2 m s^{-1} was reported from the NDBO buoy (44009) located at 38·5° N and 74·6° W. However, due to the buoy's close proximity to the coast utility of these data in representing open ocean wind conditions is questionable. Hence, for lack of any other supporting data the NMC's derived westerly wind is assumed to persist for the survey area though we must assume there to be high spatial variability in the wind field.

Figure 1. Sea surface temperature analysis from AVHRR, NOAA-10 for 13 April 1989.

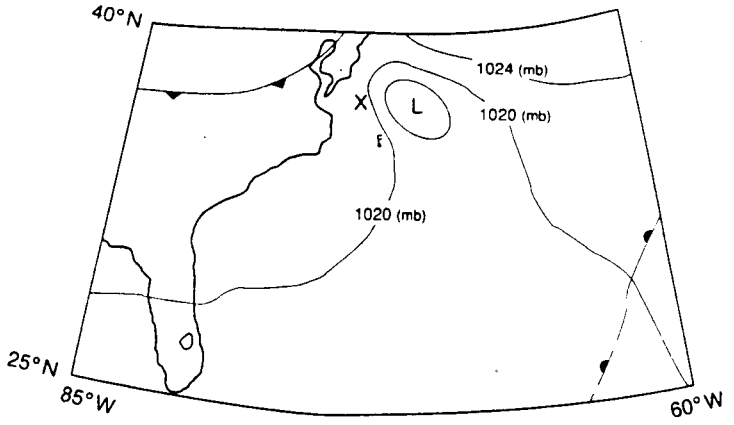

Figure 2. The NMC surface wind and pressure analysis for 13 April 1989.

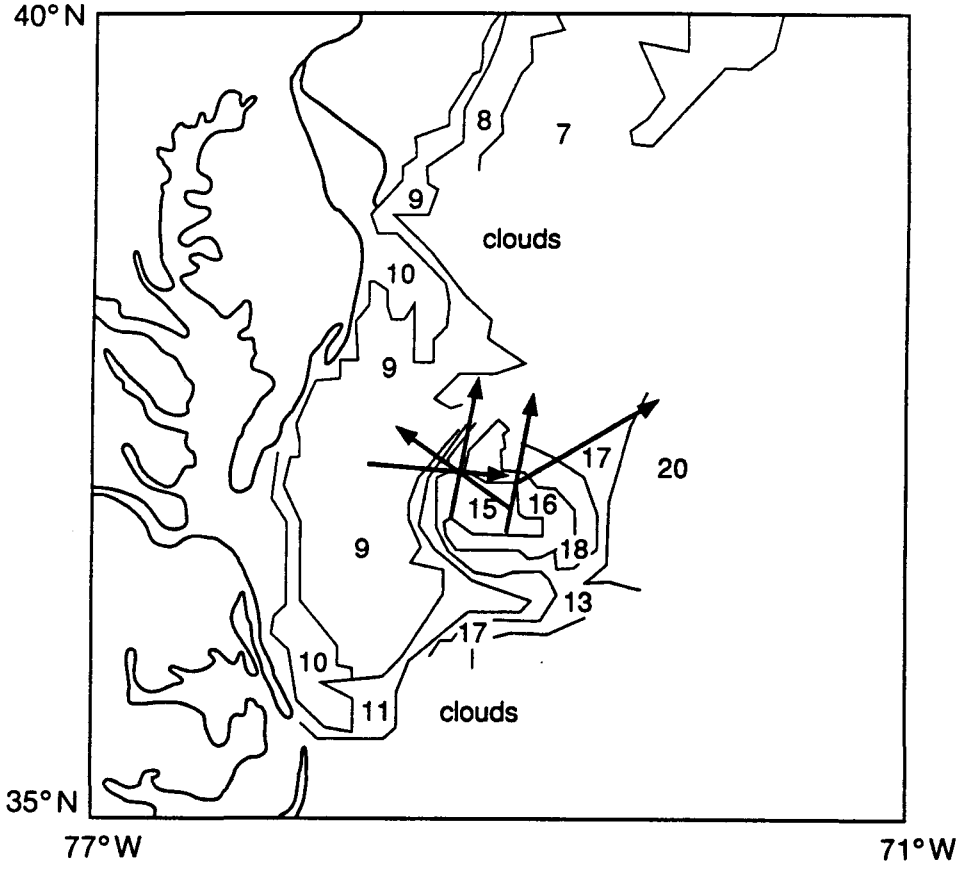

Figure 3. Sea surface temperature analysis from AVHRR, NOAA-10 for 24 April 1989.

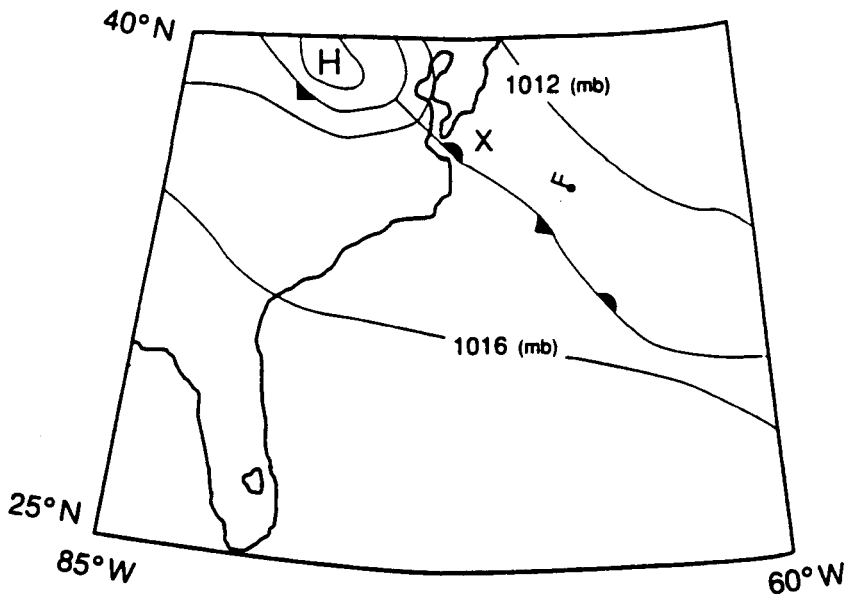

Figure 4. The NMC surface wind and pressure analysis for 25 April 1989.

3.2. *Aircraft RAR measurements*

The RAR hardware configuration, data acquisition system and processing details are given in Keller and Askari (1992). Briefly, we note that the RAR is fully calibrated to provide a measure of σ_0, the absolute radar cross-section (RCS). The radar operates incoherently transmitting and receiving a short pulse which is horizontally polarized. The pulse sweeps across a swath which actually extends from the nadir to beyond 68° (for an altitude of 1 km) in the far range. However, the effective swath where the RCS can be accurately calibrated is only 22° wide and is centred about the 45° incidence angle (figure 5). The NRL P3A is also equipped with a nadir looking pencil beam precision radiation thermometer (PRT-5) which is calibrated to give a direct measure of the alongtrack sea surface temperature with an accuracy of 0·5°C. The PRT-5 output is sampled once every second and is collected simultaneously with the RAR and the inertial navigation system measurements. Table 1 gives the pertinent instrument characteristics for the RAR and PRT-5 systems.

To determine the relation between the RCS response and the SST front, the alongtrack time series of radiometric surface temperature and RCS measurements are summarized below from the two flight days and for the different antenna look directions. We note that the RCS measurements are taken from the centre of the beam at 45° incidence angle, whereas the PRT-5 radiometer measurements are from nadir. Hence, the two time series are co-located in azimuth but are displaced in range by about 1 km.

3.2.1. *Case 1*

The flight path geometry for CASE 1 is shown in figure 6. A four-legged star pattern was flown at a 1000 m and centred at 37° 12′ N and 74° 20′ W crossing the SST front on four occasions. A total of 10 images were collected during the period

between 17.00 and 18.50 GMT. Figures 7 and 8 show the PRT-5 and RCS time-series for runs 4 and 6 taken 15 minutes apart during Case 1 and crossing the SST front with an azimuthal separation of 223°. Near surface wind direction is from the north-northwest at about 8 ms^{-1} with flow towards the warmer water. For Runs 4 the aircraft has a upwind heading of 333° (or 243° antenna look direction). For run 6, the aircraft heading is 110° downwind (or 20° antenna look direction). Due to the presence of low level clouds, the PRT-5 data is somewhat noisy but it shows (figure 7(a)) the warmer Gulf Stream waters with temperature around 20°C decreasing over the colder slope water to 10°C to 13°C, with a 7–8°C temperature differential across the front. On the basis of intercomparing the RCS and PRT-5 time-series, we note that for run 4, as the SST drops across the front, the RCS also drops by 3 dB (figure 7(b)) and the two time series are spatially in phase. In case of run 6 the RCS shows a linear trend (figure 8(b)). Finally, we note RCS variations of 5 dB for run 4 as compared to 12 dB for run 6 which occur on the length scale of 40 km, and 2 dB versus 4 dB respectively in the vicinity of the front.

3.2.2. *Case 2*

For this case a five-sided pattern centred at 37° 15′ N and 74° 15′ was flown at 1500 and 750 m (figure 9). A total of 24 images were collected during the period of 16.15 to 19.40 GMT. We will show only a portion of this data set. Figure 10 and 11 correspond to the frontal crossing for runs 15 and 17 with the aircraft heading upwind to the northeast at 330° (240° antenna look) and heading downwind to 108° (18° antenna look) respectively. The PRT-5 data (figures 10(a) 11(a)) shows a 7–8° thermal contrast across the front. The RCS measurements show a 24 dB change across the front for both runs which were taken approximately one and a half hours

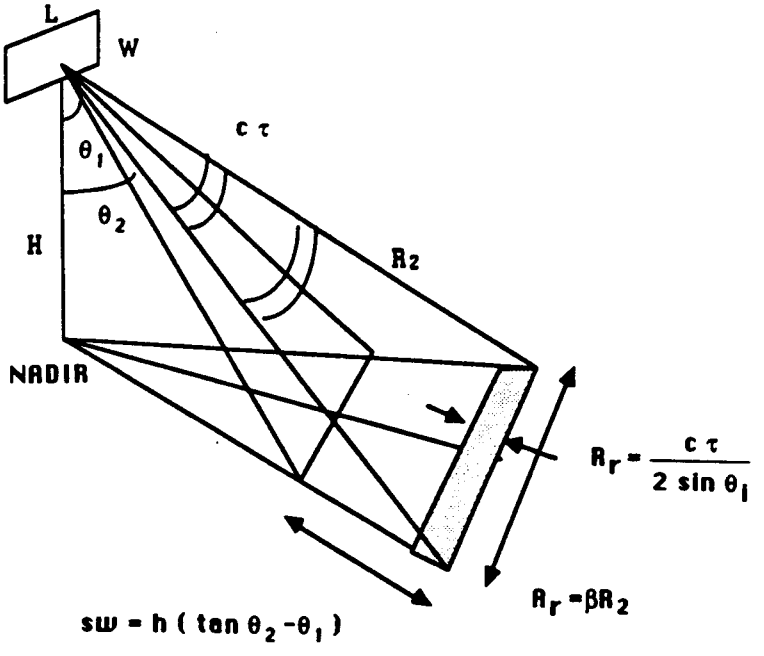

Figure 5. The RAR imaging geometry.

Table 1. Instrument characteristics.

RAR system characteristics	
Radar frequency	X-Band (9·375 GHz)
Transmit power	5 (kW)
Pulse repetition frequency (PRF)	100 (Hz)
Antenna elevation beam width	22 (degrees 3 dB)
Antenna azimuth beam width (β)	0·9 (degrees 3 dB)
Pulse width (τ)	100 (ns)
Incidence angle θ_i	45 (degrees)
Azimuth resolution (A_r)	$A_r = \frac{\beta h}{\cos \theta_i}$
Range resolution (R_r)	$R_r = \frac{c\tau}{2 \sin \theta_i}$
Swath width (SW) h = altitude, c = speed of light	$sw = h(\tan \theta_2 - \tan \theta_1]$
PRT-5 characteristics	
Instantaneous field-of-view	2 (degrees)
Atmospheric window	8–14 (μm)
Temperature accuracy	0·5 (degrees)
Alongtrack sampling rate	1 (Hz)
Incidence angle	0 (degrees nadir)

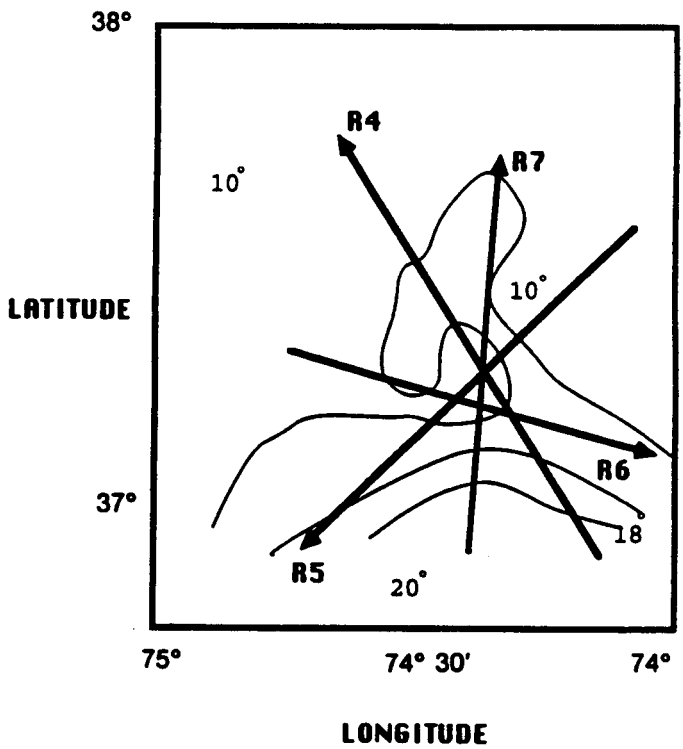

Figure 6. Flight path geometry for 13 April 1989. (R4 is the run number and 10° is temperature).

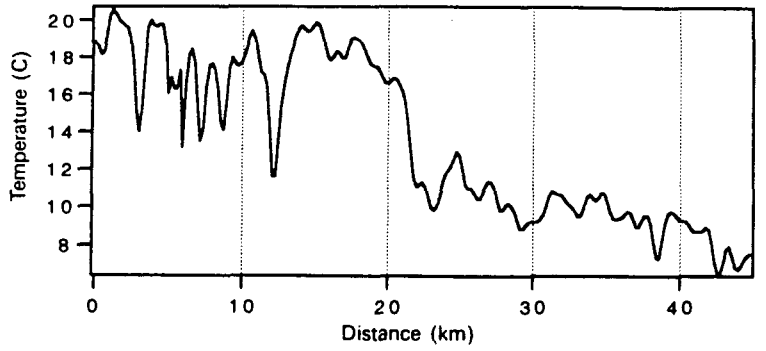

(*a*)

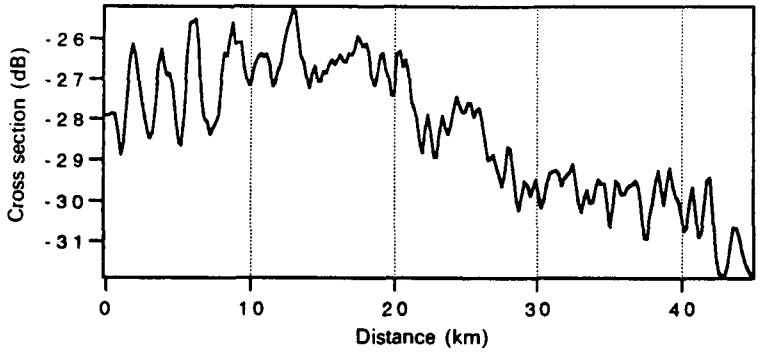

(*b*)

Figure 7 (*a*) SST time series from PRT-5 for run 4, 13 April 1989. (*b*) RCS time series taken from 45° incidence.

apart (figure 10 (b), 11 (b)). The most striking feature in both runs is that the SST front and the RCS front are separated in the azimuth by about 3 km. Actually, for both cases the RCS front, i.e., the location where a noticeable change in surface roughness occurs is upwind of the temperature front. Also, data from both runs show RCS values as low as -45 to -50 dB which are indicative of very light (on the order of 1 to 2 m s^{-1}) winds conditions.

We next show run 7, a case with a more gradual front taken inside the ring. The PRT-5 data (figure 12 (a)) shows thermal variations of the order of 3–4°C with the temperature increasing from 15° to 19°. The relative RCS change across this front is on the order of 3–4 dB with the aircraft heading cross-wind to the south-west (227°). (figure 12 (b)).

4. Discussion

In this section a descriptive account of the structure of the boundary layer in the vicinity of the front is given in order to lay groundwork for the discussions and understanding of the results from the previous section.

The difference in atmospheric stratification and buoyancy on the two sides of a sharp sea surface temperature front can create a local circulation with strong dynamic similarity to sea breeze circulations which occur at the land sea boundary.

The sea breeze circulation is driven by the gradient of atmospheric surface turbulent heat flux induced by the strength of the sea surface temperature front and the circulation is in turn coupled to the ambient large scale flow. However, one expects the ambient flow to intensify or diminish the localized effect depending on the ambient wind speed and direction relative to the local flow. For example for low wind ambient conditions and strong SST fronts, a feedback mechanism develops where upward convective motion over the warmer water causes a low level wind to blow towards the warmer side of the SST front thereby extending the domain of circulation or the evolution of the boundary layer both downstream and upstream of the front (figure 13(a)). For runs 15 and 17 during the 25 April experiment, radar observations showed RCS changes as large as 25 dB across the temperature front which are indicative of light winds in a heterogeneous environment, furthermore it was shown that wind fronts due to the 'sea breeze' type of convergences could be detected as sharp gradients in radar cross-section and were found a few kilometres away from the sea surface temperature front.

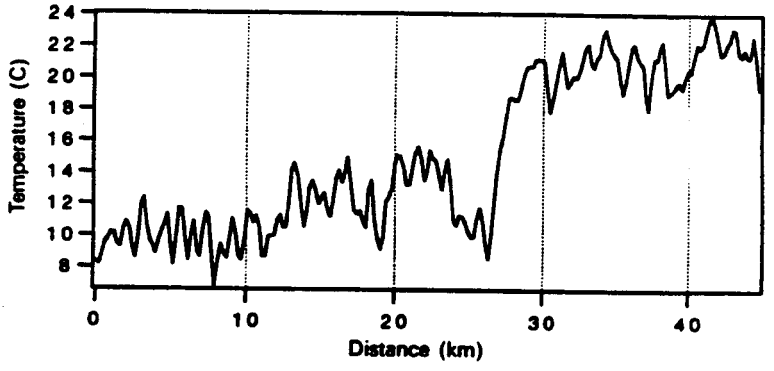

(*a*)

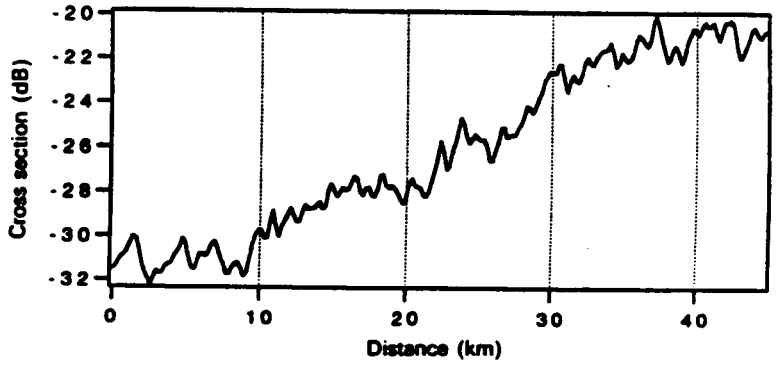

(*b*)

Figure 8 (*a*) SST time series from PRT-5 for run 6, 13 April 1989. (*b*) RCS time series taken from 45° incidence.

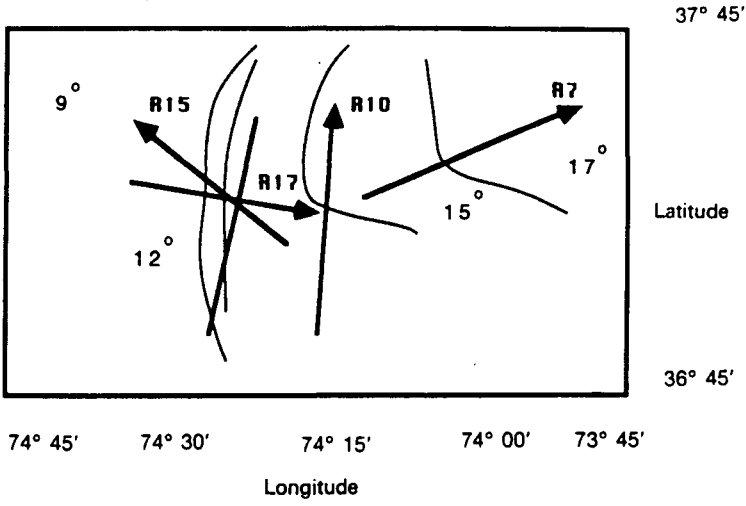

Figure 9. Flight path geometry for 25 April 1989. (R15 is the run number and 12° is temperature).

In the moderate to high wind speeds cases (runs 4 and 6 13 April) with flow perpendicular to the front, the circulatory cell will likely migrate downstream; in this case, an internal boundary layer (IBL) will form in the downstream side of the SST front with its depth increasing gradually with distance downwind. While even in this case a step-function in wind stress is observed over the SST front, the gradual growth in the IBL produces a gradual change in surface stress so that its asymptotic value is not achieved until the IBL reaches the depth of the full boundary layer (figure 13(b)). For weaker sea surface temperature fronts, as was the case with run 7 on 25 April, the horizontal change in atmospheric heat fluxes is small enough that no discernible circulation could be generated which could compete with the large scale wind field, and no discernible wind front was observed using the real aperture radar.

There are numerous examples of boundary layer characteristics in the vicinity of temperature discontinuities. Wind tunnel studies simulating the stratified atmospheric flow over a heat island (a heat source creating a large temperature discontinuity inside the tunnel) have shown that circulation cells can indeed exist both upwind and downwind of the heat island, generating a three-dimensional flow with lateral surface convergence, upward vertical motion, and upper-level divergence (Raman and Cermak 1975). Similar boundary layer structures have been observed by Raynor *et al.* (1975) in airflow conditions from land to water and water to land. Recent studies of buoyancy-driven sea breeze circulations by Holt and Raman (1990) and Wayland and Raman (1989) in the vicinity of the Gulf Stream have shown that, in the vicinity of a SST front, there can be both a change in wind speed and direction. In fact the acceleration effect due to the low-level convergence process can result in a factor of two increase in the wind speed over the warmer water. Numerical modelling results of Huang and Raman (1988) demonstrated that low level convergence (opposing wind vectors) and a sharp increase of u^* can occur

downwind of a strong SST front in addition to the sharp change in u^* near the SST front.

What seems to be emerging is that the RCS variations across the front are largely dependent on the local wind direction with respect to the front and the change in wind stress due to both surface layer response at the front and feedbacks from the larger scale buoyancy-driven circulations.

A variety of other factors may be contributing to the observed changes in the RCS, most notably the accumulation of surfactants or surface films at the frontal region. Figure 14 is the RAR image corresponding to run 15 of the frontal crossing on 25 April as discussed in the previous section. The image has an azimuthal extent of about 30 km; the 0 and 45° incidence angles are marked in the range direction. The image shows the RCS variability with a weak front at 16 km and a second front with noticeable change in surface roughness occurring at about 19 km. The two fronts are parallel in range but displaced by 3 km in the azimuth. The first front was identified by the nadir looking PRT-5 as the location of the thermal front. Also shown are a series of dark red parallel streaks running in the range direction which could possibly be related to the presence of surface films. Surfactants collected along the convergence regions of fronts can drastically dampen the short gravity and

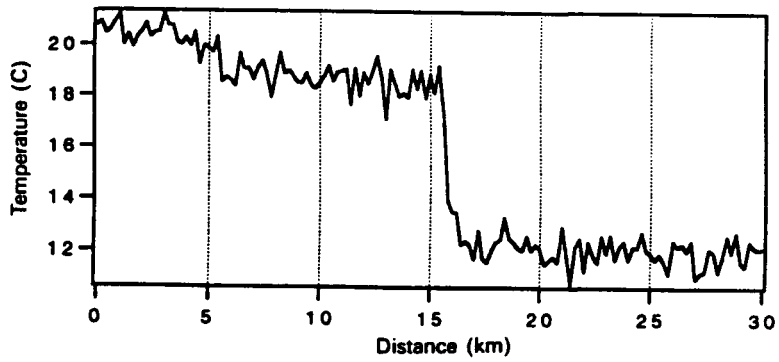

(*a*)

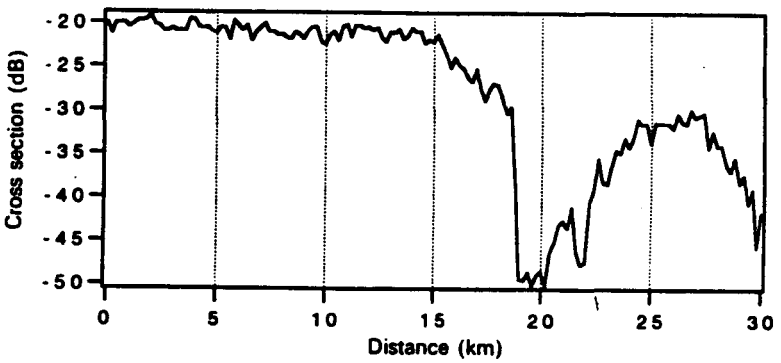

(*b*)

Figure 10 (*a*) SST time series from PRT-5 for run 15, 25 April 1989. (*b*) RCS time series taken from 45° incidence.

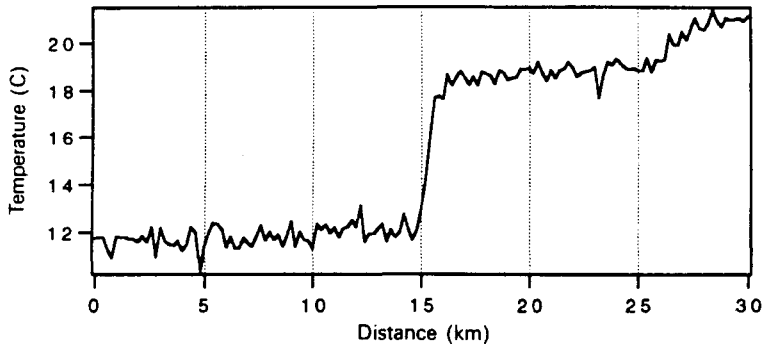

(*a*)

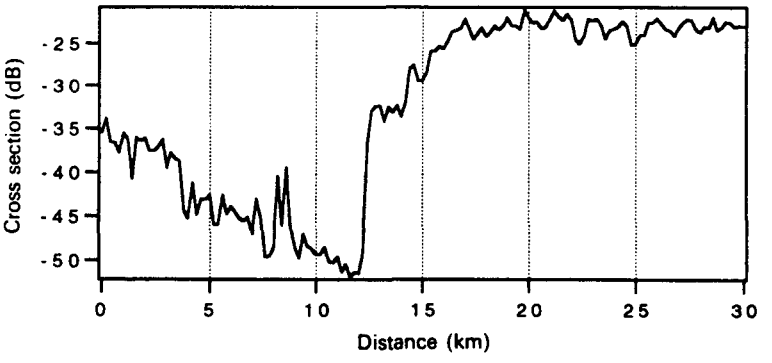

(*b*)

Figure 11 (*a*) SST time series from PRT-5 for run 17, 25 April 1989. (*b*) RCS time series taken from 45° incidence.

capillary waves which are responsible for Bragg scattering and in effect reduce the RCS. At this time, we do not have a quantitative handle on the natural surfactant variability at the front; Huhnerfuss *et al.* 1983 and Alpers and Huhnerfuss 1989 provide some experimental as well as theoretical insight into this difficult problem.

Among other processes which enter into modulations of radar backscatter are wave-wave and wave-current interactions causing spectral perturbations of resonance Bragg waves. Shear and or diverging currents are frequently found along ocean fronts. The gradients associated with these currents can modify the surface short wave spectrum, hence the radar backscatter through hydrodynamic stretching and straining or tilt modulations (Askari *et al.* 1992, Thompson *et al.* 1988, Gasparovic *et al.* 1988, Lyzenga and Bennett 1988). Furthermore, as discussed by Sheres *et al.* (1985) shear currents can act like low pass filters refracting the slower short waves and allowing the fast moving long waves to pass through a front thereby creating differences in dominant wavelengths, wave slopes and wave age on opposite sides of a front. The change in wave age and its relation to wind speed, wind direction and the neutral drag coeficient was discussed by (Geernaert *et al.* 1986, Li *et al.* 1989, Raman 1978).

5. Conclusions

This research suggests that in the presence of light to moderate winds in the neighbourhood of sharp SST fronts, several sharp gradients in RAR imagery may be observed: gradients due to the surface layer wind stress response to local stratification at the SST front; and also a roughness change dislocated from the SST front which is associated with the horizontal extent of the sea breeze which is in turn driven by the SST front.

During both flight days of the RAR experiments, imagery were collected without the luxury of complementary *in situ* observations of the marine boundary layer local wind fields or the ocean surface properties. Due to the lack of other information, wind direction was derived from surface weather maps and assumed to remain constant throughout the region. Explanations of multiple fronts in the RAR images are provided in terms of the current understanding of atmospheric boundary layer (ABL) response to SST fronts.

Unfortunately, ABL theory rests on similarity assumptions which require that the field be horizontal homogeneous and stationary; therefore, our ability to model the local wind stress field in heterogeneous environments relies on existing and

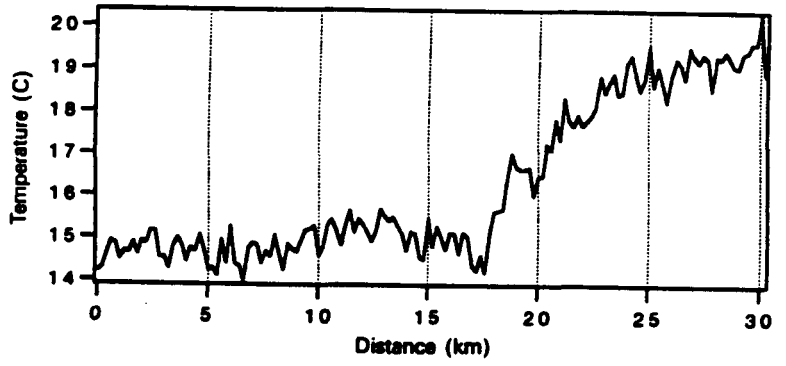

(*a*)

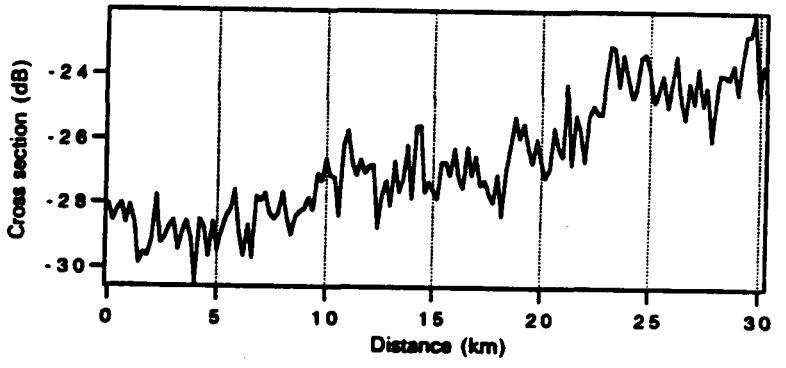

(*b*)

Figure 12 (*a*) SST time series from PRT-5 for run 7, 25 April 1989. (*b*) RCS time series taken from 45° incidence.

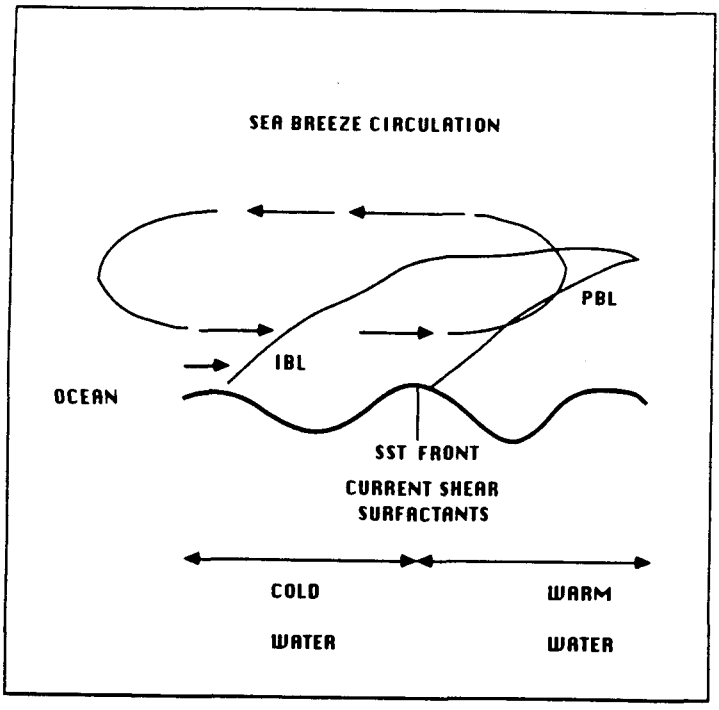

(*a*)

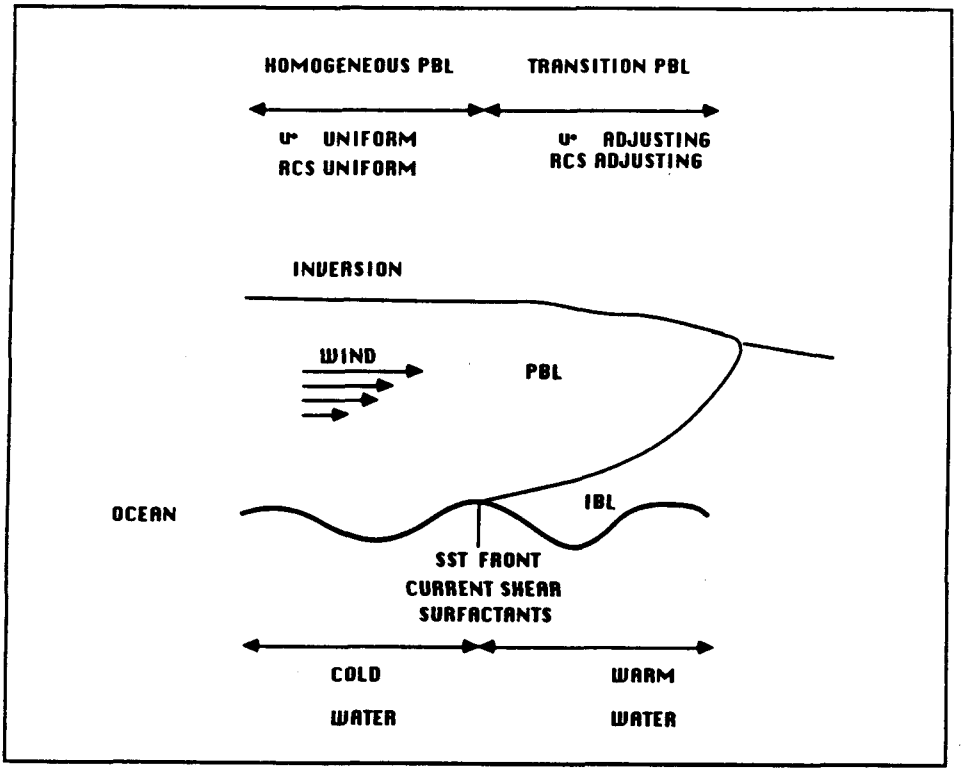

(*b*)

Figure 13 (*a*) Pictorial of the sea breeze circulation in the vicinity of a sea surface temperature front. (*b*) Pictorial of the adjusting boundary layer in the vicinity of a sea-surface temperature front.

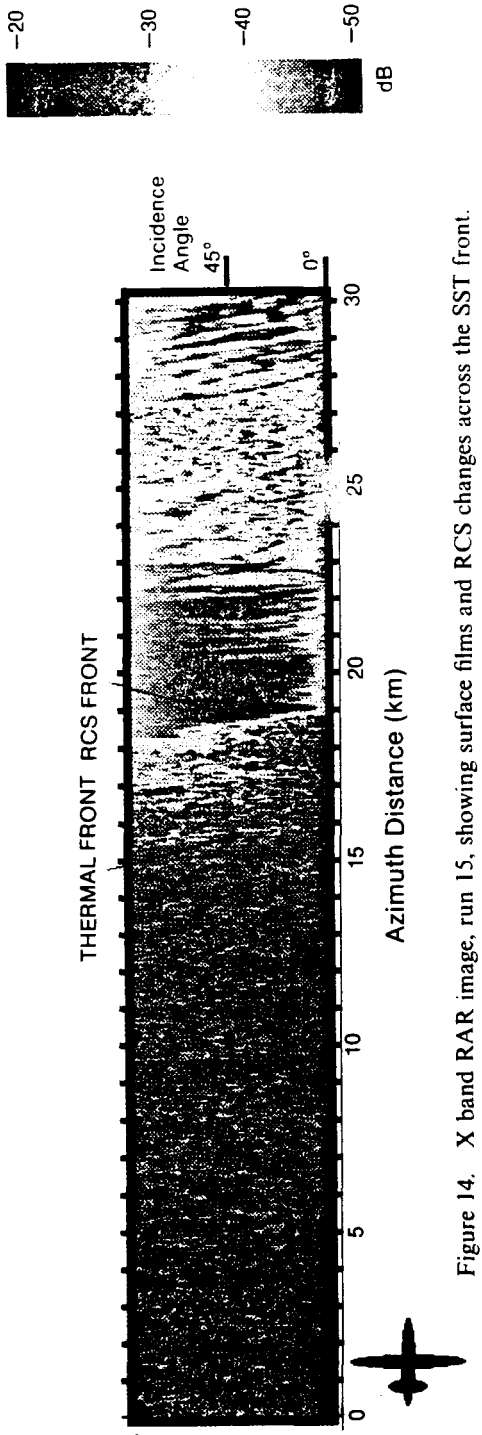

Figure 14. X band RAR image, run 15, showing surface films and RCS changes across the SST front.

future research results in the ocean-atmosphere interactions. Progress in understanding the large heterogeneity and multiple fronts imaged by radars will rest in the synergy and coordination in the ocean, atmosphere, and remote sensing disciplines.

Acknowledgments

This research was supported by the High Resolution Remote Sensing Accelerated Research Initiative of the Naval Research Laboratory. We would like to thank Mrs Jennifer Clark of NOAA for providing the sea surface temperature analysis (figures 1 and 3).

References

ALPERS, W., and HUHNERFUSS, H., 1989, The damping of ocean waves by surface films: A new look at an old problem. *Journal of Geophysical Research*, **94**, 6251-6265.

ASKARI, F., KELLER, W. C., LYZENGA, D. R., and BENNETT, J. R., 1992, An estuarine front viewed by an imaging radar. Submitted to *Journal of Geophysical Research*.

CHENEY, R. E., 1981, A search for cold water rings. Spaceborne SAR for oceanography. In *Spaceborne Synthetic Aperture Radar for Oceanography*, edited by R. C. Beal, P. S. DeLeonibus and I. Katz (Baltimore, London: The Johns Hopkins University Press), pp. 161-170.

DONELAN, M. A., and PIERSON, W. J., 1987, Radar scattering and equilibrium ranges in wind-generated waves with application to scatterometry. *Journal of Geophysical Research*, **92**, 4971-5029.

FU, L. L., and HOLT, B., 1983, Some examples of detection of oceanic mesoscale eddies by the Seasat SAR. *Journal of Geophysical Research*, **88**, 1844-1852.

GASPAROVIC, R. F., APEL, J. R. and KASISCHKE, E. S., 1988, An overview of the SAR internal wave signature experiment. *Journal of Geophysical Research*, **93**, 12304-12316.

GEERNAERT, G. L., KATSAROS, K. B., and RICHTER, K., 1986, Variation of the drag coefficient and its dependence on sea state. *Journal of Geophysical Research*, **91**, 7667-7679.

GEERNAERT, G. L., PLANT, W. J., and SCHULER, D., 1988, K_u-band NRCS measurements and their dependence on wind azimuth, wave state, wind stress, and wind speed during FASINEX. *Proceedings of the Seventh Conference on Ocean Atmosphere Interaction, held in Anaheim, CA, on 1-5 February 1988*, (Boston, MA: American Meteorological Society), pp. 111-114.

GEERNAERT, G. L., 1990a, Influence of coastal fetch-limited waves on determining the wind stress during diabatic conditions, In *Proceedings of the Conference on Turbulence and Diffusion. Roskilde, Denmark* (Boston: American Meteorological Society).

GEERNAERT, G. L., 1990b, Bulk parameterization for the wind stress and heat fluxes. In *Surface Waves and Fluxes Current Theory and Remote Sensing*, edited by G. L. Geernaert and W. J. Plant (The Netherlands: Kluwer Academic Publishers), pp. 92-173.

HAYES, R. M., 1981, Detection of the Gulf Stream. Spaceborne SAR for oceanography. In *Spaceborne Synthetic Aperture Radar for Oceanography*, edited by R. C. Beal, P. S. DeLeonibus and I. Katz (Baltimore, London: The Johns Hopkins University Press), pp. 146-160.

HOLT, T., and RAMAN, S., 1990, Marine boundary-layer structure and circulation in the region of offshore redevelopment of a cyclone during GALE. *Monthly Weather Review*, **118**, 392-410.

HUANG, C. Y., and RAMAN, S., 1988, A numerical modelling study of the marine boundary layer over the Gulf Stream during cold air advection. *Boundary-layer Meteorology*, **45**, 251-290.

HUHNERFUSS, H., ALPERS, W., CROSS, A., GARRET, W. D., KELLER, W. C., LANGE P. A., PLANT, W. J., SCHLUDE, F., and SCHULER, D. L., 1983, The modification of X and L band radar signals by monomolecular sea slicks. *Journal of Geophysical Research*, **88**, 9817-9822.

KELLER, M., and PLANT, W. J., 1988, X-band scatterometer measurements at low winds in a wave tank. *Proceedings of the Seventh Conference on Ocean Atmosphere Interaction,*

held in Anaheim, CA, on 1-5 February (Boston, MA: American Meteorological Society), pp. J41-J43.

KELLER, W. C., WISMANN, V., and ALPERS, W., 1989, Tower-based measurements of the ocean C-band radar cross-section. *Journal of Geophysical Research*, **94**, 924-930.

KELLER, W. C., and ASKARI, F., 1992, *Naval Research Laboratory's Real Time, Real Aperture Radar: The System and its Applications*. In preparation.

LI, F., LARGE, W. G., SHAW, W. J., WALSH, E., and DAVIDSON, K., 1989, Ocean radar backscatter relationship with near-surface winds. *Journal of Physical Oceanography*, **19**, 342-353.

LICHY, D. E., MATTIE, M. G., and MANCINI, L. J., 1981, Tracking of a warm water ring. In *Spaceborne Synthetic Aperture Radar for Oceanography*, edited by R. C. Beal, P. S. DeLeonibus and I. Katz (Baltimore, London: The Johns Hopkins Univertsity Press), pp. 171-184.

LYZENGA, D. R., and BENNETT, J. R., 1988, Full-Spectrum modelling of synthetic aperture radar internal wave signatures. *Journal of Geophysical Research*, **93**, 12345-12354.

PLANT, W. J., 1986, A two-scale model of short wind-generated waves and scatterometry. *Journal of Geophysical Research*, **91**, 10735-10749.

PLANT, W. J., 1990, Bragg scattering of electromagnetic waves from the air/sea interface. In *Surface Waves and Fluxes Current Theory and Remote Sensing*, edited by G. L. Geernaert and W. J. Plant (The Netherlands: Kluwer Academic Publishers), pp. 375-442.

RAMAN, S., AND CERMAK, J. E., 1975, Mean temperature and mean concentration distributions over a physically modelled three-dimensional heat island for different stability conditions. *Boundary-Layer Meteorology*, **9**, 427-440.

RAMAN, S., 1978, Influence of mean wind direction on sea surface wave development. *Journal of Physical Oceanography*, **8**, 926-929.

RAYNOR, G. S., MICHAEL, P., BROWN, R. M., and RAMAN, S., 1975, Studies of atmospheric diffusion from a nearshore oceanic site. *Journal of Applied Meteorology*, **14**, 1080-1094.

ROSS, D. B., 1981, The wind speed dependency of ocean microwave backscatter. In *Spaceborne Synthetic Aperture Radar for Oceanography*, edited by R. C. Beal, P. S. DeLeonibus and I. Katz (Baltimore, London: The Johns Hopkins University Press), pp. 75-86.

SCHROEDER, L. C., BOGGS, D. H., DOME, G., HALBERSTAM, I. M., JONES, W. L., PIERSON, W. J., and WENTZ, F. J. 1982, The relationship between wind vector and normalized radar cross-section used to derive Seasat-A satellite scatterometer winds. Seasat Special Issue I, *Journal of Geophysical Research*, **87**, 3318-3336.

STAGE, S. A., and WELLER, R. A., 1985, The Frontal Air-Sea Interaction Experiment (FASINEX); Part 1: Background and scientific objectives. *Bulletin American Meteorological Society*, **66**, 1511-1520.

STAGE, S. A., and WELLER, R. A., 1986, The Frontal Air-Sea Interaction Experiment (FASINEX); Part 2: Experimental Plan. *Bulletin American Meterological Society*, **67**, **16-20.**

SHERES, D., KENYON, K. E., BERNSTEIN, R. L., and BEARDLEY, R. C., 1985, Large horizontal surface velocity shears in the ocean obtained from images of refracting swell and *in situ* moored current data. *Journal of Geophysical Research*, **90**, 4943-4950.

SMITH, S. D., 1980, Wind Stress and heat flux over the ocean in gale force winds. *Journal of Physical Oceanography*, **10**, 709-726.

THOMPSON, D. R., 1988, Calculation of radar backscatter modulations from internal waves. *Journal of Geophysical Research*, **93**, 12371-14132.

WAYLAND, R. J., and RAMAN, S., 1989, Mean and turbulent structure of a baroclinic marine boundary layer during the 28 January 1986 cold-air outbreak (GALE 86). *Boundary-layer Meteorology*, **48**, 227-254.

WEISSMAN, D. E., and THOMPSON, T. W., 1977, Detection and interpretation of ocean roughness variations across the Gulf Stream inferred from radar cross section observations. In *Oceans '77 Conference Proceedings*, held in Los Angeles, California on 17-19 October 1977, pp. 14B1-14B10.